Defect process, dopant behaviour and Li ion mobility in the Li 2 MnO 3 cathode material

Kuganathan, N., Sgourou, E. N., Panayiotatos, Y. & Chroneos, A.

Original citation:
Kuganathan, N, Sgourou, EN, Panayiotatos, Y & Chroneos, A 2019, 'Defect process, dopant behaviour and Li ion mobility in the Li 2 MnO 3 cathode material', Energies, vol. 12, no. 7, 1329.
https://dx.doi.org/10.3390/en12071329

DOI 10.3390/en12071329
ESSN 1996-1073

Publisher: MDPI

energies

MDPI

Article

Defect Process, Dopant Behaviour and Li Ion Mobility in the Li_2MnO_3 Cathode Material

Navaratnarajah Kuganathan [1,2,*], Efstratia N. Sgourou [3,4], Yerassimos Panayiotatos [4] and Alexander Chroneos [1,2]

1 Department of Materials, Imperial College London, London SW72AZ, UK; alexander.chroneos@imperial.ac.uk or ab8104@coventry.ac.uk
2 Faculty of Engineering, Environment and Computing, Coventry University, Priory Street, Coventry CV15FB, UK
3 Solid State Physics Section, University of Athens, Panepistimiopolis Zografos, 15784 Athens, Greece; e_sgourou@hotmail.com
4 Department of Mechanical Engineering, University of West Attica, 12210 Athens, Greece; gpana@uniwa.gr
* Correspondence: n.kuganathan@imperial.ac.uk or ad0636@coventry.ac.uk

Received: 6 March 2019; Accepted: 2 April 2019; Published: 7 April 2019

Abstract: Lithium manganite, Li_2MnO_3, is an attractive cathode material for rechargeable lithium ion batteries due to its large capacity, low cost and low toxicity. We employed well-established atomistic simulation techniques to examine defect processes, favourable dopants on the Mn site and lithium ion diffusion pathways in Li_2MnO_3. The Li Frenkel, which is necessary for the formation of Li vacancies in vacancy-assisted Li ion diffusion, is calculated to be the most favourable intrinsic defect (1.21 eV/defect). The cation intermixing is calculated to be the second most favourable defect process. High lithium ionic conductivity with a low activation energy of 0.44 eV indicates that a Li ion can be extracted easily in this material. To increase the capacity, trivalent dopants (Al^{3+}, Co^{3+}, Ga^{3+}, Sc^{3+}, In^{3+}, Y^{3+}, Gd^{3+} and La^{3+}) were considered to create extra Li in Li_2MnO_3. The present calculations show that Al^{3+} is an ideal dopant for this strategy and that this is in agreement with the experiential study of Al-doped Li_2MnO_3. The favourable isovalent dopants are found to be the Si^{4+} and the Ge^{4+} on the Mn site.

Keywords: Li_2MnO_3; defects; Li diffusion; dopants

1. Introduction

The next generation of high capacity energy storage systems require lithium ion cathode material exhibiting high energy density, low cost and non-toxicity. A variety of cathode materials have been examined in the past decade to improve the performance of the rechargeable Li ion batteries [1–11]. As very few of them exhibit promising results, there is a necessity to make breakthroughs in finding new materials.

"Layered" Li_2MnO_3 was recently investigated as a potential cathode material for Li ion batteries due to its high theoretical capacity of 285 $mAhg^{-1}$ and first charge plateau of ~4.5 eV [12,13]. Furthermore, manganese is relatively safe, abundant and low-cost, making Li_2MnO_3 a very promising cathode material. However, the material suffered from poor structural stability during cycling and electrical conductivity [14,15]. Li_2MnO_3 was initially identified as an inactive material because the electrochemical activity of the material via the oxidation of Mn^{4+} to Mn^{5+} did not occur [16,17]. The electrochemical activity was reinvestigated later and it was determined that the extraction and reinsertion of Li is possible. Chen et al. [18] showed that theoretically Li extraction can be charge compensated by the formation of O_2 from O^{2-} ions in the lattice. Cho et al. [19] demonstrated

that oxygen loss is energetically favourable during delithiation. Electrochemical performance was recently examined by doping Al on the Mn site, and it was shown that Al-doped Li_2MnO_3 exhibits an enhancement on the rate capability and cycling stability [20].

To optimize the performance of Li ion batteries, a more detailed fundamental understanding of existing materials is necessary. Computational modelling techniques have significantly contributed to the characterization of experimental structures, prediction of pathways of migrating ions and identification of promising dopants in a variety of oxide materials [21–36]. In the present study, we examine the intrinsic defects process, Li ion diffusion paths and the effect of dopants on the Mn site in Li_2MnO_3.

2. Computational Methods

Static atomistic calculations were performed on the crystal structure of Li_2MnO_3 and its defect structures using the General Utility Lattice Program (GULP) code [37]. This method is based on the classical Born model of ionic crystals. Interactions between ions include the long-range (i.e., Coulombic) ionic interactions and the short-range (i.e., electron–electron repulsion and van der Waals interactions) ionic interactions, with both being considered. Short-range repulsive forces were modelled using the Buckingham potentials (refer to Supplementary Information). The Broyden–Fletcher–Goldfarb–Shanno (BFGS) algorithm [38] was applied to relax atom positions and lattice constants. In all optimized structures, forces on the atoms were smaller than 0.001 eV/Å. The point defects and migrating atoms were modelled using the Mott–Littleton method [39]. In this method, two spherical regions are defined, with the inner spherical region containing a number of ions greater than 700. In this region, ions are relaxed explicitly. Defect enthalpies in this simulation are expected to be overestimated as the ions are treated as spherical shapes with full charge at dilute limit. However, relative energies and trends remain consistent.

From a thermodynamic viewpoint, the defect parameters (for example, migration and formation energies) can be defined via the comparison of the real (defective) crystal to an isobaric or isochoric ideal (non-defective) crystal. These sets of defect formation parameters can be interconnected through thermodynamic relations as discussed in previous studies [40,41]. Here, the atomic scale calculations correspond to the isobaric parameters for the migration and formation processes [42,43].

3. Results

3.1. Bulk Li_2MnO_3 Structure

Figure 1 shows the experimentally observed crystal structure of Li_2MnO_3. This structure belongs to the monoclinic structure of the C2/m space group (lattice parameters a = 4.937 Å, b = 8.532 Å, c = 5.030 Å, $\alpha = 90.0^\circ$, $\beta = 109.46^\circ$ and $\gamma = 90.0^\circ$) as reported by Strobel et al. [44] in their single crystal X-ray diffraction. The crystal structure of Li_2MnO_3 was subsequently reinvestigated by Boulineau et al. [45] and their reported structure was closer to the previous structure, with a small amount of cation mixing. Here, we used the crystal structure reported by Strobel et al. [44], as this model consisted of full occupancy atom positions. Both Li and Mn form edge-sharing distorted octahedral units with adjacent O atoms, as shown in the Figure 1.

Both atom positions and lattice constants were allowed to relax under constant pressure to obtain the equilibrium lattice structure. The calculated lattice constants were in excellent agreement with the experimental values, as reported in Table 1.

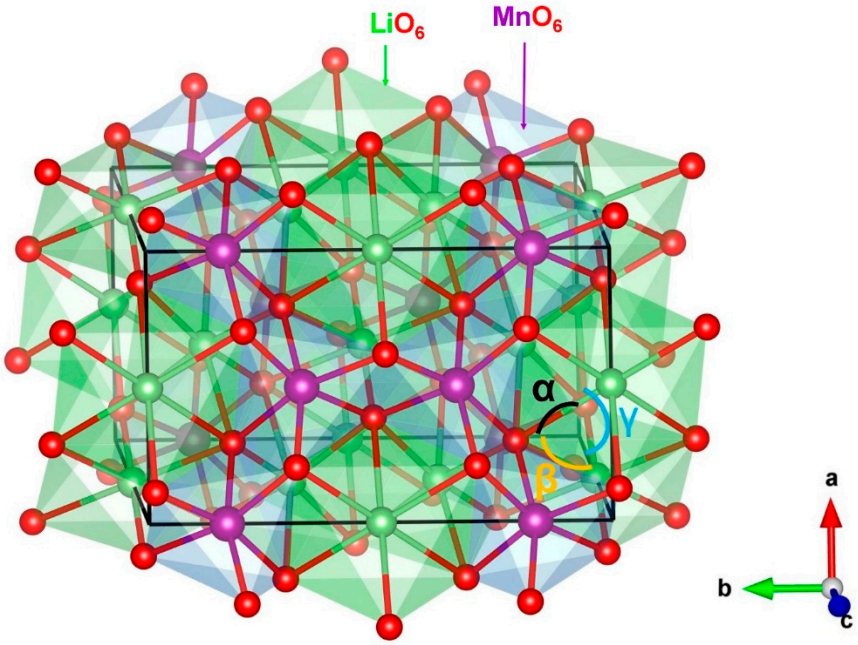

Figure 1. Crystal structure of Li_2MnO_3 (space group C 2/m).

Table 1. Calculated structural parameters and corresponding experimental values [44] reported for monoclinic (C2/m) Li_2MnO_3.

Parameter	Calculated	Experiment [44]	| Δ | (%)
a (Å)	4.8715	4.9370	1.33
b (Å)	8.3519	8.5320	2.11
c (Å)	5.0177	5.0300	0.24
α (°)	90.0	90.0	0.00
β (°)	110.07	109.46	0.56
γ (°)	90.0	90.0	0.00

3.2. Intrinsic Defect Processes

Next, defect formation energies for the isolated vacancy, interstitial and anti-site defect were calculated, and were combined to calculate the Frenkel, Schottky and anti-site intrinsic defect reaction energies (Equations (1)–(8)). Intrinsic defect processes are useful to study the electrochemical behaviour of Li_2MnO_3. The following reactions, which were written by using Kröger–Vink notation [46], represent the Frenkel, Schottky and anti-site intrinsic defect processes:

$$\text{Li Frenkel} : \mathrm{Li}_{\mathrm{Li}}^{\mathrm{X}} \rightarrow V_{\mathrm{Li}}^{\prime} + \mathrm{Li}_{\mathrm{i}}^{\bullet} \quad (1)$$

$$\text{Mn Frenkel} : V_{\mathrm{Mn}}^{\mathrm{X}} \rightarrow V_{\mathrm{Mn}}^{\prime\prime\prime\prime} + \mathrm{Mn}_{\mathrm{i}}^{\bullet\bullet\bullet\bullet} \quad (2)$$

$$\text{O Frenkel} : \mathrm{O}_{\mathrm{O}}^{\mathrm{X}} \rightarrow V_{\mathrm{O}}^{\bullet\bullet} + \mathrm{O}_{\mathrm{i}}^{\prime\prime} \quad (3)$$

$$\text{Schottky} : 2\mathrm{Li}_{\mathrm{Li}}^{\mathrm{X}} + \mathrm{Mn}_{\mathrm{Mn}}^{\mathrm{X}} + 3\mathrm{O}_{\mathrm{O}}^{\mathrm{X}} \rightarrow 2V_{\mathrm{Li}}^{\prime} + V_{\mathrm{Mn}}^{\prime\prime\prime\prime} + 3V_{\mathrm{O}}^{\bullet\bullet} + \mathrm{Li}_2\mathrm{MnO}_3 \quad (4)$$

$$\mathrm{Li}_2\mathrm{O\ Schottky} : 2\mathrm{Li}_{\mathrm{Li}}^{\mathrm{X}} + \mathrm{O}_{\mathrm{O}}^{\mathrm{X}} \rightarrow 2V_{\mathrm{Li}}^{\prime} + V_{\mathrm{O}}^{\bullet\bullet} + \mathrm{Li}_2\mathrm{O} \quad (5)$$

$$\mathrm{MnO}_2\mathrm{Schottky} : \mathrm{Mn}_{\mathrm{Mn}}^{\mathrm{X}} + 2\mathrm{O}_{\mathrm{O}}^{\mathrm{X}} \rightarrow V_{\mathrm{Mn}}^{\prime\prime\prime\prime} + 2V_{\mathrm{O}}^{\bullet\bullet} + \mathrm{MnO}_2 \quad (6)$$

$$\text{Li/Mn antisite (isolated)} : \mathrm{Li}_{\mathrm{Li}}^{\mathrm{X}} + \mathrm{Mn}_{\mathrm{Mn}}^{\mathrm{X}} \rightarrow \mathrm{Li}_{\mathrm{Mn}}^{\prime\prime\prime} + \mathrm{Mn}_{\mathrm{Li}}^{\bullet\bullet\bullet} \quad (7)$$

$$\text{Li/Mn antisite (cluster)} : \mathrm{Li}_{\mathrm{Li}}^{\mathrm{X}} + \mathrm{Mn}_{\mathrm{Mn}}^{\mathrm{X}} \rightarrow \left\{\mathrm{Li}_{\mathrm{Mn}}^{\prime\prime\prime} : \mathrm{Mn}_{\mathrm{Li}}^{\bullet\bullet\bullet}\right\}^{\mathrm{X}} \quad (8)$$

We report the reaction energies for these intrinsic defect processes in Figure 2. The Li Frenkel was calculated to be the most thermodynamically favourable intrinsic defect process. This process increases the concentration of Li vacancies that can enhance vacancy-assisted Li ion diffusion in Li_2MnO_3. Other Frenkel defect processes exhibit highly endoergic energies, suggesting that they are unlikely to occur at operating temperatures. The second most favourable defect process is the Li–Mn anti-site. In this defect, a small percentage of Li on Mn sites ($Li_{Mn}^{'''}$) and Mn on Li sites ($Mn_{Li}^{\bullet\bullet\bullet}$) would be observed at high temperatures. Anti-site defect has been observed in experimental and theoretical studies during the synthesis of as-prepared material and cycling [47–52]. The Li_2O Schottky reaction (Equation (5)), leading to the formation of further $V_{Li}^{'}$ and $V_{O}^{\bullet\bullet}$, is 5.16 eV per defect, indicating that this reaction can only take place at high temperatures.

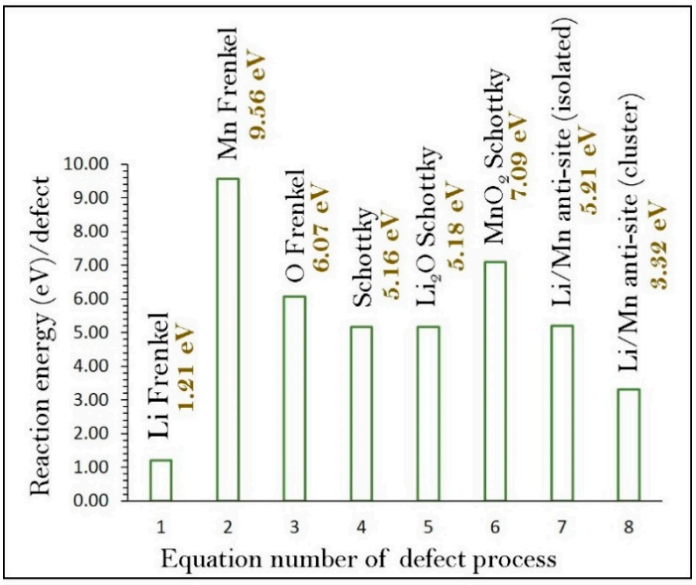

Figure 2. Energetics of intrinsic defect process calculated in monoclinic Li_2MnO_3.

3.3. Lithium Ion Diffusion

There is a necessity to understand the lithium ion diffusion paths together with activation energies to assess Li_2MnO_3 as a potential high-capacity cathode material for Li ion batteries. Determining Li ion diffusion paths is extremely challenging experimentally. Classical pair potential-based simulation can provide valuable information about various possible Li ion diffusion paths and corresponding activation energies. Low activation energy is a key requirement for a promising high-rate battery material. Possible Li vacancy-assisted diffusion paths were constructed. Six different local Li hops (Figure 3) were identified for the Li vacancy migration. Table 2 reports the Li–Li separation, together with corresponding activation energies. Figure 4 shows the energy profile diagrams for activation energies of local Li hops.

Five possible long-range paths consisting of local Li hops with lower overall activation energies were identified (Table 3). The first long-range path (intra layer along the *b* axis) exhibited a slightly distorted linear pattern (A→E→E→A), with an overall activation energy of 0.59 eV. The second path connected local hops B and F, forming a curved trajectory (F→B→B→B) along the *ab* plane (intra layer), with an overall activation energy of 0.47 eV. The third long-range path (C→C→C→C) lay between layers (inter layer), with the Li local hops of C. The activation energy for this migration was calculated to be 0.44 eV. This was the lowest activation energy of the four intra layer Li migration paths. In the fourth long-range path (D→D→D→D), the Li ion migrated in the *bc* plane (intra layer), with an overall migration energy of 0.45 eV. Finally, the fifth long-range path (D→D→D→D) was located in the *ab* plane (intra layer) and the activation energy for this path was 0.47 eV. The current results show that the Li ion would diffuse fast in Li_2MnO_3 via intra layers or inter layers.

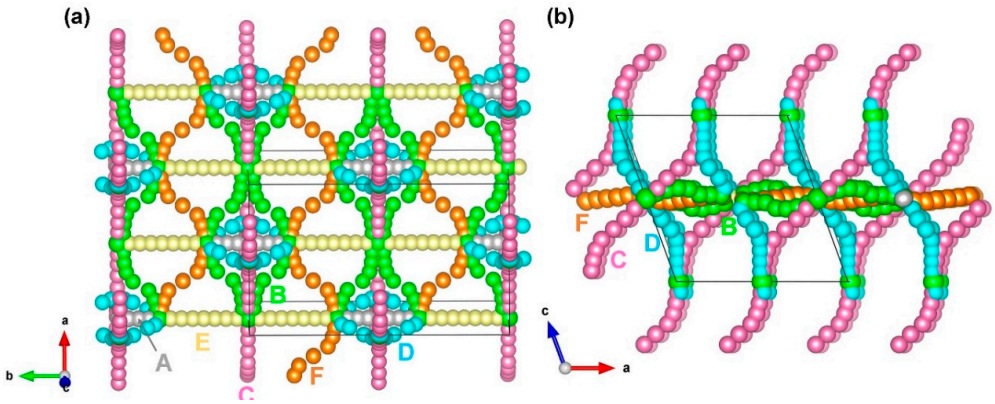

Figure 3. Different Li trajectory views (**a**) and (**b**) possible long-range lithium vacancy migration paths considered. Yellow, light blue, purple, green, grey and light brown color atoms correspond to different Li hopping trajectories.

Table 2. Calculated Li–Li separations and activation energies using classical pair-potential method for the lithium ion migration between two adjacent Li sites (as shown in Figure 3).

Migration Path	Li–Li Separation (Å)	Activation Energy (eV)
A	2.65	0.27
B	2.77	0.37
C	2.83	0.44
D	2.84	0.45
E	2.85	0.59
F	2.87	0.47

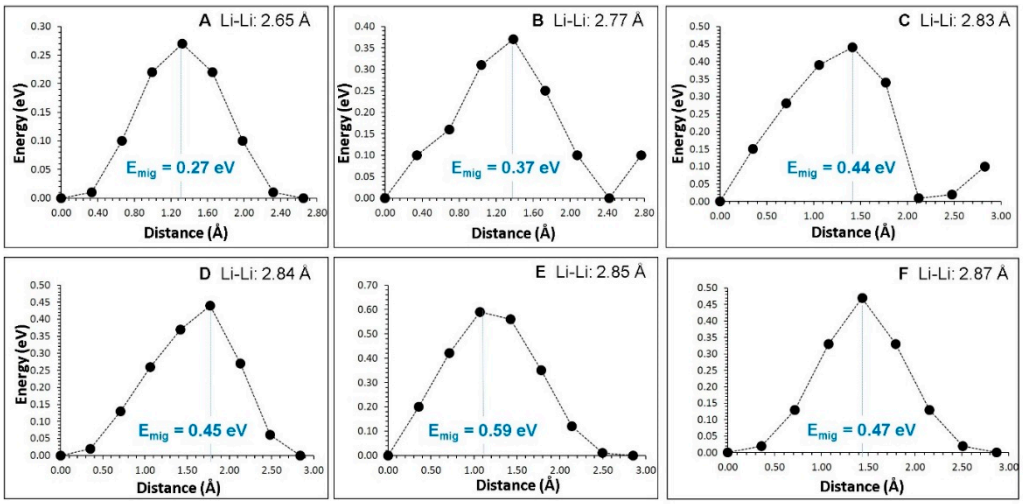

Figure 4. Six different energy profiles (as shown in Figure 3) of Li vacancy hopping between two adjacent Li sites in Li_2MnO_3.

Table 3. Possible long-range Li ion diffusion paths and their corresponding overall activation energies.

Long-Range Path	Direction	Overall Activation Energy (eV)
A→E→E→A	*b* axis	0.59
F→B→B→ B	*ab* plane	0.47
C→C→C→C	*ac* plane	0.44
D→D→D→D	*bc* plane	0.45
F→F→F→F	*ab* plane	0.47

3.4. Trivalent Doping

The capacity of Li_2MnO_3 can be increased by incorporating additional Li in the form of interstitials into the as-prepared crystal structure. This would increase its applicability in rechargeable lithium batteries. Doping trivalent cations on the Mn site is an efficient engineering strategy to create Li interstitials in the lattice. In previous work, this strategy has been applied to Li and Na ion battery materials. In this work, we considered some trivalent dopants from different parts of the periodic table (early transition elements, post-transition elements and lanthanide elements). The selection of the prominent dopant Al^{3+} is due to its small size and low cost. Furthermore, there is an experimental report on the doping of Al^{3+} on the Mn site [20]. The solution of R_2O_3 (R = Al, Co, Ga, Sc, In, Y, Gd and La) was considered via the following process (in Kröger–Vink notation):

$$R_2O_3 + 2Mn_{Mn}^{X} + Li_2O \rightarrow 2R'_{Mn} + 2Li_i^{\bullet} + 2MnO_2 \quad (9)$$

Figure 5 reports the solution enthalpies of R_2O_3 calculated using the classical pair-potential method. The present calculations show that the most favourable dopant on the Mn site is Al^{3+}. This indicates that the extra lithium can be incorporated in the form of interstitials into Li_2MnO_3. The exact concentration of the composition can be provided by an experimental study. The possible composition of Al-doped Li_2MnO_3 is $Li_{2+x}Mn_{1-x}Al_xO_3$ (x = 0.0, . . . , 1.0).

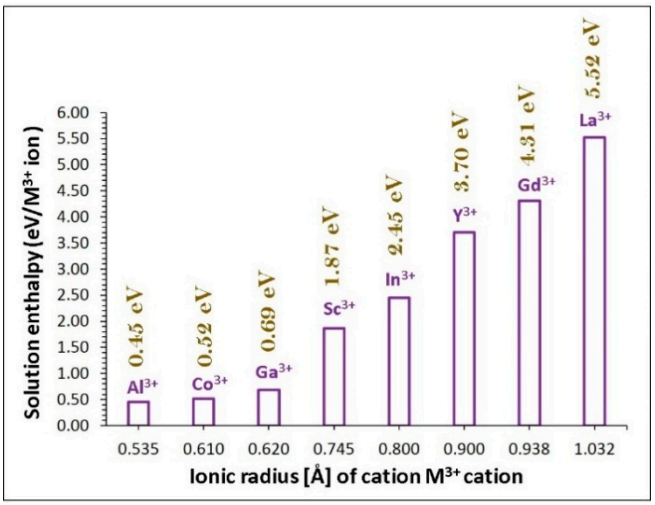

Figure 5. Enthalpy of solution of R_2O_3 (R = Al, Co, Ga, Sc, In, Y, Gd and La) with respect to the R^{3+} ionic radius in Li_2MnO_3.

Xiang et al. [20] synthesised both Li_2MnO_3 and Al-doped Li_2MnO_3 and examined their rate capacities. Their study shows that there is a greater improvement in the Al-doped Li_2MnO_3 compared with that of pristine Li_2MnO_3. The second most favourable dopant is the Co^{3+} and its solution enthalpy is calculated to be 0.52 eV, only 0.07 eV higher than that of Al^{3+}. Solution enthalpy increases gradually with the ionic radius of M^{3+} ions reflecting in the bond lengths and bond angles. The optimised bond lengths and bond angles of trivalent dopants occupying the Mn site and the octahedral MnO_6 unit in the relaxed structure of undoped Li_2MnO_3 are shown in Figure 6. The highest solution enthalpy is calculated for La^{3+}. This is due to the larger ionic radius difference between the La^{3+} and the Mn^{4+}. The current solution enthalpy values for Sc^{3+}, In^{3+}, Y^{3+}, Gd^{3+} and La^{3+} are highly endoergic, suggesting that they are unfavourable at operating temperatures.

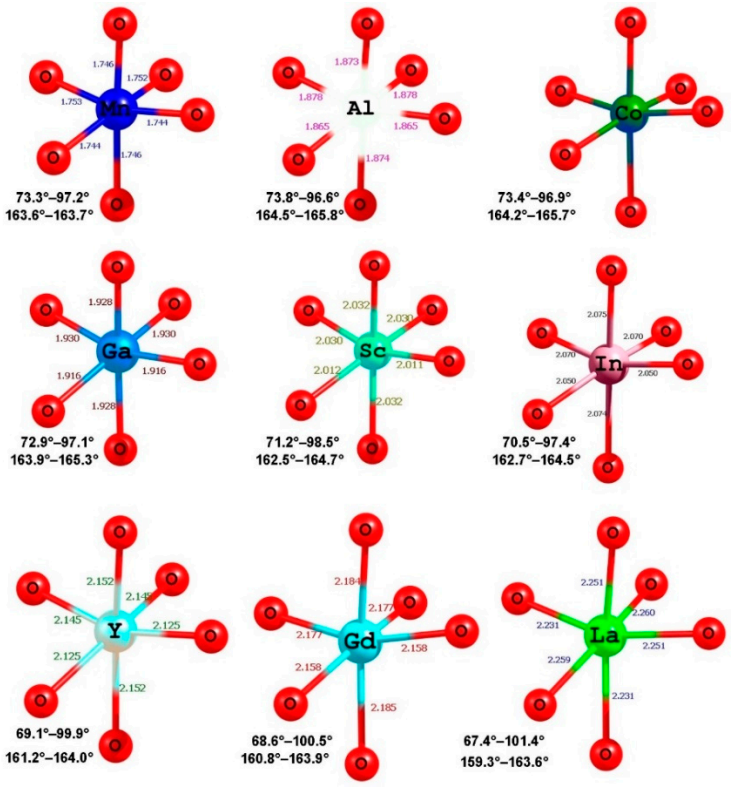

Figure 6. Distorted octahedral MnO_6 units in the relaxed structure of undoped Li_2MnO_3.

Density functional theory calculations performed by Hoang et al. [53] show that Al and Fe are energetically favourable dopants on the Mn site, which agrees with our calculations. Kong et al. [54] used *ab* initio simulations to examine the thermodynamical stability of a variety of aliovalent dopants, including trivalent dopants Al^{3+} and Fe^{3+} on the Mn site. In their study, charge introduced by cation doping was compensated by anion doping (F and N) on the O site. In our study, negative charge introduced by trivalent dopants on the Mn site was compensated by positively charged Li interstitials, creating a Li_2MnO_3 material with a high capacity.

3.5. Tetravalent Doping

Here, we consider some isovalent dopants (Si^{4+}, Ge^{4+}, Ti^{4+}, Sn^{4+}, Zr^{4+} and Ce^{4+}) on the Mn site. The following reaction equation was used to calculate the solution enthalpy:

$$MO_2 + Mn^X_{Mn} \rightarrow M^X_{Mn} + MnO_2 \quad (10)$$

Solution enthalpy increases with ionic radius. Exoergic solution enthalpy was calculated for Si^{4+} and Ge^{4+} (Figure 7). This was due to the smaller ionic radius of Si^{4+} (0.40 Å) compared with Mn^{4+} (0.53 Å). The higher charge density of Si^{4+} forms stronger Si–O bonds, as reported in Figure 8. The ionic radii of Ge^{4+} and Mn^{4+} are the same. This is reflected in the exoergic solution enthalpy. The optimised structures of MO_6 units together with bond lengths and bond angles are shown in Figure 8. Endoergic solution enthalpies are observed for the other dopants. Solution enthalpy for CeO_2 is highly endoergic, meaning that doping Ce on the Mn site is highly unlikely to occur.

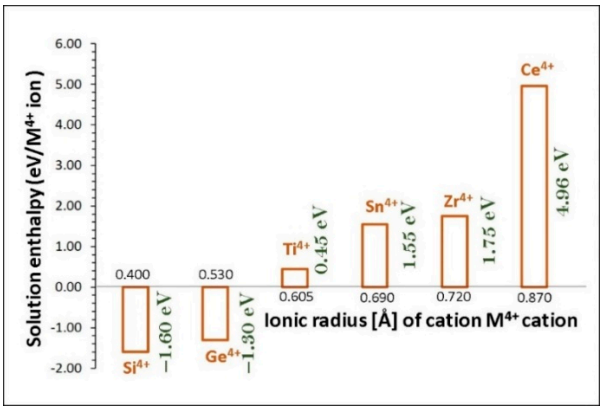

Figure 7. Enthalpy of solution of RO_2 (R = Si, Ge, Ti, Sn, Zr and Ce) with respect to the R^{4+} ionic radius in Li_2MnO_3.

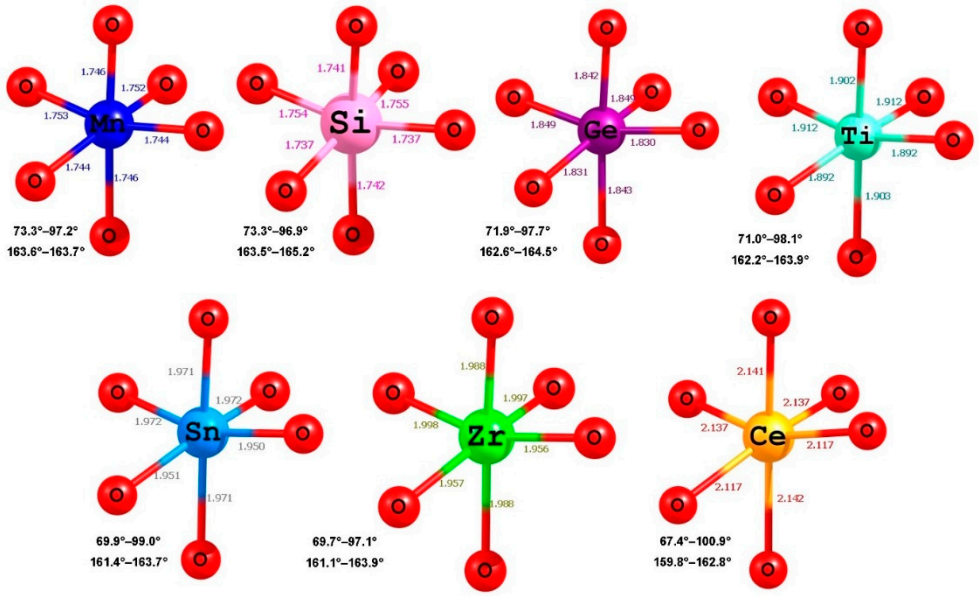

Figure 8. Distorted octahedral MnO_6 units in the relaxed structure of undoped Li_2MnO_3 and the coordination formed by the isovalent (tetravalent) dopants on the Mn site with neighbour oxygen.

4. Conclusions

In conclusion, we have used atomistic simulation techniques to examine intrinsic defects, Li ion diffusion pathways with activation energies and favourable trivalent and tetravalent dopants on the Mn site in Li_2MnO_3. The lowest defect energy process was calculated to be the Li Frenkel, which will ensure the number of Li vacancies that are necessary for vacancy-assisted Li diffusion. The second most favourable defect process was found to be the cation mixing. Diffusion of lithium with the low activation energy of 0.44 eV suggests that high ionic conductivity would be observed in Li_2MnO_3. Doping of Al on the Mn site is an efficient strategy to increase the Li content, as reported in the experiment. The favourable isovalent dopants were calculated to be the Si^{4+} and Ge^{4+}. These theoretical predictions require experimental verification.

Supplementary Materials: The following are available online at http://www.mdpi.com/1996-1073/12/7/1329/s1, Table S1: Interatomic potential parameters used in the atomistic simulations of Li_2MnO_3.

Author Contributions: Computation, N.K.; writing, N.K.; analysis and editing, E.N.S., Y.P. and A.C.

Funding: The research leading to these results received funding from the European Union's H2020 Programme under Grant Agreement no 824072–HARVESTORE.

Acknowledgments: We acknowledge the computational facilities and support provided by the High Performance Computing Center at Imperial College.

Conflicts of Interest: The authors declare no conflict of interest.

References

1. Armand, M.; Tarascon, J.M. Building better batteries. *Nature* **2008**, *451*, 652. [CrossRef] [PubMed]
2. Whittingham, M.S. Lithium batteries and cathode materials. *Chem. Rev.* **2004**, *104*, 4271–4302. [CrossRef] [PubMed]
3. Padhi, A.K.; Nanjundaswamy, K.S.; Goodenough, J.B. Phospho-olivines as positive-electrode materials for rechargeable lithium batteries. *J. Electrochem. Soc.* **1997**, *144*, 1188–1194. [CrossRef]
4. Nytén, A.; Abouimrane, A.; Armand, M.; Gustafsson, T.; Thomas, J.O. Electrochemical performance of Li_2FeSiO_4 as a new Li-battery cathode material. *Electrochem. Commun.* **2005**, *7*, 156–160. [CrossRef]
5. Nishimura, S.-I.; Hayase, S.; Kanno, R.; Yashima, M.; Nakayama, N.; Yamada, A. Structure of Li_2FeSiO_4. *J. Am. Chem. Soc.* **2008**, *130*, 13212–13213. [CrossRef]
6. Armstrong, A.R.; Kuganathan, N.; Islam, M.S.; Bruce, P.G. Structure and lithium transport pathways in li_2fesio_4 cathodes for lithium batteries. *J. Am. Chem. Soc.* **2011**, *133*, 13031–13035. [CrossRef]
7. Masquelier, C.; Croguennec, L. Polyanionic (phosphates, silicates, sulfates) frameworks as electrode materials for rechargeable Li (or Na) batteries. *Chem. Rev.* **2013**, *113*, 6552–6591. [CrossRef]
8. Wang, J.; Zhang, G.; Liu, Z.; Li, H.; Liu, Y.; Wang, Z.; Li, X.; Shih, K.; Mai, L. $Li_3V(MoO_4)_3$ as a novel electrode material with good lithium storage properties and improved initial coulombic efficiency. *Nano Energy* **2018**, *44*, 272–278. [CrossRef]
9. Recham, N.; Chotard, J.N.; Dupont, L.; Delacourt, C.; Walker, W.; Armand, M.; Tarascon, J.M. A 3.6 V lithium-based fluorosulphate insertion positive electrode for lithium-ion batteries. *Nat. Mater.* **2009**, *9*, 68. [CrossRef] [PubMed]
10. Afyon, S.; Wörle, M.; Nesper, R. A lithium-rich compound $Li_7Mn(BO_3)_3$ containing Mn2+ in tetrahedral coordination: A cathode candidate for lithium-ion batteries. *Angew. Chemie Inter. Ed.* **2013**, *52*, 12541–12544. [CrossRef] [PubMed]
11. Nishimura, S.-I.; Nakamura, M.; Natsui, R.; Yamada, A. New lithium iron pyrophosphate as 3.5 V class cathode material for lithium ion battery. *J. Am. Chem. Soc.* **2010**, *132*, 13596–13597. [CrossRef] [PubMed]
12. Thackeray, M.M.; Johnson, C.S.; Vaughey, J.T.; Li, N.; Hackney, S.A. Advances in manganese-oxide 'composite' electrodes for lithium-ion batteries. *J. Mater. Chem.* **2005**, *15*, 2257–2267. [CrossRef]
13. Goodenough, J.B.; Kim, Y. Challenges for rechargeable Li batteries. *Chem. Mater.* **2010**, *22*, 587–603. [CrossRef]
14. Rana, J.; Stan, M.; Kloepsch, R.; Li, J.; Schumacher, G.; Welter, E.; Zizak, I.; Banhart, J.; Winter, M. Structural changes in Li_2MnO_3 cathode material for Li-ion batteries. *Adv. Energy Mater.* **2014**, *4*, 1300998. [CrossRef]
15. Francis Amalraj, S.; Markovsky, B.; Sharon, D.; Talianker, M.; Zinigrad, E.; Persky, R.; Haik, O.; Grinblat, J.; Lampert, J.; Schulz-Dobrick, M.; et al. Study of the electrochemical behavior of the "inactive" Li_2MnO_3. *Electrochim. Acta* **2012**, *78*, 32–39. [CrossRef]
16. Ammundsen, B.; Paulsen, J. Novel lithium-ion cathode materials based on layered manganese oxides. *Adv. Mater.* **2001**, *13*, 943–956. [CrossRef]
17. Robertson, A.D.; Bruce, P.G. The origin of electrochemical activity in Li_2MnO_3. *Chem. Commun.* **2002**, 2790–2791. [CrossRef]
18. Chen, H.; Islam, M.S. Lithium extraction mechanism in Li-Rich Li_2MnO_3 involving oxygen hole formation and dimerization. *Chem. Mater.* **2016**, *28*, 6656–6663. [CrossRef]
19. Cho, E.; Kim, K.; Jung, C.; Seo, S.-W.; Min, K.; Lee, H.S.; Park, G.-S.; Shin, J. Overview of the oxygen behavior in the degradation of Li_2MnO_3 cathode material. *J. Phys. Chem. C* **2017**, *121*, 21118–21127. [CrossRef]
20. Xiang, Y.; Wu, X. Enhanced electrochemical performances of Li_2MnO_3 cathode materials by Al doping. *Ionics* **2018**, *24*, 83–89. [CrossRef]
21. Kuganathan, N.; Islam, M.S. Li_2MnSiO_4 lithium battery material: Atomic-scale study of defects, lithium mobility, and trivalent dopants. *Chem. Mater.* **2009**, *21*, 5196–5202. [CrossRef]
22. Fisher, C.A.J.; Kuganathan, N.; Islam, M.S. Defect chemistry and lithium-ion migration in polymorphs of the cathode material Li_2MnSiO_4. *J. Mater. Chem. A* **2013**, *1*, 4207–4214. [CrossRef]

23. Kuganathan, N.; Kordatos, A.; Anurakavan, S.; Iyngaran, P.; Chroneos, A. Li_3SbO_4 lithium-ion battery material: Defects, lithium ion diffusion and tetravalent dopants. *Mater. Chem. Phys.* **2019**, *225*, 34–41. [CrossRef]
24. Kordatos, A.; Kuganathan, N.; Kelaidis, N.; Iyngaran, P.; Chroneos, A. Defects and lithium migration in Li_2CuO_2. *Sci. Rep.* **2018**, *8*, 6754. [CrossRef] [PubMed]
25. Kuganathan, N.; Chroneos, A. Defects, dopants and sodium mobility in Na_2MnSiO_4. *Sci. Rep.* **2018**, *8*, 14669. [CrossRef]
26. Kuganathan, N.; Chroneos, A. Defects and dopant properties of $Li_3V_2(PO_4)_3$. *Sci. Rep.* **2019**, *9*, 333. [CrossRef] [PubMed]
27. Kuganathan, N.; Ganeshalingam, S.; Chroneos, A. Defects, dopants and lithium mobility in $Li_9V_3(P_2O_7)_3(PO_4)_2$. *Sci. Rep.* **2018**, *8*, 8140. [CrossRef] [PubMed]
28. Kuganathan, N.; Iyngaran, P.; Chroneos, A. Lithium diffusion in Li_5FeO_4. *Sci. Rep.* **2018**, *8*, 5832. [CrossRef]
29. Kuganathan, N.; Kordatos, A.; Chroneos, A. Li_2SnO_3 as a cathode material for lithium-ion batteries: Defects, lithium ion diffusion and dopants. *Sci. Rep.* **2018**, *8*, 12621. [CrossRef]
30. Kuganathan, N.; Kordatos, A.; Chroneos, A. Defect chemistry and Li-ion diffusion in Li_2RuO_3. *Sci. Rep.* **2019**, *9*, 550. [CrossRef] [PubMed]
31. Kuganathan, N.; Kordatos, A.; Kelaidis, N.; Chroneos, A. Defects, lithium mobility and tetravalent dopants in the Li_3NbO_4 cathode material. *Sci. Rep.* **2019**, *9*, 2192. [CrossRef] [PubMed]
32. Kuganathan, N.; Kordatos, A.; Fitzpatrick, M.E.; Vovk, R.V.; Chroneos, A. Defect process and lithium diffusion in Li_2TiO_3. *Solid State Ionics* **2018**, *327*, 93–98. [CrossRef]
33. Kuganathan, N.; Tsoukalas, L.H.; Chroneos, A. Defects, dopants and Li-ion diffusion in Li_2SiO_3. *Solid State Ionics* **2019**, *335*, 61–66. [CrossRef]
34. Araújo, C.M.; Blomqvist, A.; Scheicher, R.H.; Chen, P.; Ahuja, R. Superionicity in the hydrogen storage material Li_2NH: Molecular dynamics simulations. *Phys. Rev. B* **2009**, *79*, 172101. [CrossRef]
35. Seymour, I.D.; Chroneos, A.; Kilner, J.A.; Grimes, R.W. Defect processes in orthorhombic $LnBaCo_2O_{5.5}$ double perovskites. *Phys. Chem. Chem. Phys.* **2011**, *13*, 15305–15310. [CrossRef] [PubMed]
36. Jay, E.E.; Rushton, M.J.D.; Chroneos, A.; Grimes, R.W.; Kilner, J.A. Genetics of superionic conductivity in lithium lanthanum titanates. *Phys. Chem. Chem. Phys.* **2015**, *17*, 178–183. [CrossRef] [PubMed]
37. Gale, J.D.; Rohl, A.L. The general utility lattice program (GULP). *Molec. Simul.* **2003**, *29*, 291–341. [CrossRef]
38. Gale, J.D. GULP: A computer program for the symmetry-adapted simulation of solids. *J. Chem. Soc. Faraday Trans.* **1997**, *93*, 629–637. [CrossRef]
39. Mott, N.F.; Littleton, M.J. Conduction in polar crystals. I. Electrolytic conduction in solid salts. *Trans. Faraday Soc.* **1938**, *34*, 485–499. [CrossRef]
40. Varotsos, P. Defect volumes and the equation of state in α-PbF_2. *Phys. Rev. B* **2007**, *76*, 092106. [CrossRef]
41. Varotsos, P. Comparison of models that interconnect point defect parameters in solids with bulk properties. *J. Appl. Phys.* **2007**, *101*, 123503. [CrossRef]
42. Chroneos, A.; Vovk, R.V. Modeling self-diffusion in UO_2 and ThO_2 by connecting point defect parameters with bulk properties. *Solid State Ionics* **2015**, *274*, 1–3. [CrossRef]
43. Chroneos, A. Connecting point defect parameters with bulk properties to describe diffusion in solids. *Appl. Phys. Rev.* **2016**, *3*, 041304. [CrossRef]
44. Strobel, P.; Lambert-Andron, B. Crystallographic and magnetic structure of Li_2MnO_3. *J. Solid State Chem.* **1988**, *75*, 90–98. [CrossRef]
45. Boulineau, A.; Croguennec, L.; Delmas, C.; Weill, F. Reinvestigation of Li_2MnO_3 structure: Electron diffraction and high resolution TEM. *Chem. Mater.* **2009**, *21*, 4216–4222. [CrossRef]
46. Kröger, F.A.; Vink, H.J. Relations between the concentrations of imperfections in crystalline solids. In *Solid State Physics*; Seitz, F., Turnbull, D., Eds.; Academic Press: New York, NY, USA, 1956; Volume 3, pp. 307–435.
47. Politaev, V.V.; Petrenko, A.A.; Nalbandyan, V.B.; Medvedev, B.S.; Shvetsova, E.S. Crystal structure, phase relations and electrochemical properties of monoclinic Li_2MnSiO_4. *J. Solid State Chem.* **2007**, *180*, 1045–1050. [CrossRef]
48. Ensling, D.; Stjerndahl, M.; Nytén, A.; Gustafsson, T.; Thomas, J.O. A comparative XPS surface study of Li_2FeSiO_4/C cycled with LiTFSI- and $LiPF_6$-based electrolytes. *J. Mater. Chem.* **2009**, *19*, 82–88. [CrossRef]

49. Liu, H.; Choe, M.-J.; Enrique, R.A.; Orvañanos, B.; Zhou, L.; Liu, T.; Thornton, K.; Grey, C.P. Effects of antisite defects on li diffusion in $LiFePO_4$ revealed by Li isotope exchange. *J. Phys. Chem. C* **2017**, *121*, 12025–12036. [CrossRef]
50. Kempaiah Devaraju, M.; Duc Truong, Q.; Hyodo, H.; Sasaki, Y.; Honma, I. Synthesis, characterization and observation of antisite defects in $LiNiPO_4$ nanomaterials. *Sci. Rep.* **2015**, *5*, 11041. [CrossRef]
51. Kuganathan, N.; Chroneos, A. $Na_3V(PO_4)_2$ cathode material for Na ion batteries: Defects, dopants and Na diffusion. *Solid State Ionics* **2019**, *336*, 75–79. [CrossRef]
52. Kuganathan, N.; Iyngaran, P.; Vovk, R.; Chroneos, A. Defects, dopants and Mg diffusion in $MgTiO_3$. *Sci. Rep.* **2019**, *9*, 4394. [CrossRef] [PubMed]
53. Hoang, K. Doping Li-rich cathode material Li_2MnO_3: Interplay between lattice site preference, electronic structure, and delithiation mechanism. *Phys. Rev. Mater.* **2017**, *1*, 075404. [CrossRef]
54. Kong, F.; Longo, R.C.; Park, M.-S.; Yoon, J.; Yeon, D.-H.; Park, J.-H.; Wang, W.-H.; Kc, S.; Doo, S.-G.; Cho, K. Ab initio study of doping effects on $LiMnO_2$ and Li_2MnO_3 cathode materials for Li-ion batteries. *J. Mater. Chem. A* **2015**, *3*, 8489–8500. [CrossRef]